remote sensing

MDPI

Article

Rising Net Shortwave Radiation and Land Surface Temperature Drive Snow Cover Phenology Shifts Across the Mongolian Plateau During the 2000–2022 Hydrological Years

Xiaona Chen [1,2,*] and Shiqiu Lin [1,3]

[1] State Key Laboratory of Resources and Environmental Information System, Institute of Geographic Sciences and Natural Resources Research, Chinese Academy of Sciences, Beijing 100101, China; linshiqiu0016@igsnrr.ac.cn
[2] National Earth System Science Data Center, Beijing 100101, China
[3] College of Resources and Environment, University of Chinese Academy of Sciences, Beijing 101408, China
* Correspondence: chenxn@igsnrr.ac.cn

Abstract

Snow cover phenology (SCP) serves as a critical regulator of hydrological cycles and ecosystem stability across the Mongolian Plateau (MP). Despite its importance, the spatiotemporal patterns of SCP and their climatic drivers remain poorly quantified, constrained by persistent gaps in satellite snow cover observations. Leveraging a high-resolution (500 m) daily gap-filled Moderate Resolution Imaging Spectroradiometer (MODIS) snow cover dataset combined with reanalysis climate datasets, we systematically quantified SCP dynamics and identified the dominant controls during the 2000–2022 hydrological years using trend analysis and ridge regression. Our results reveal a significant divergence in SCP parameters: snow end dates (D_e) advanced markedly across the entire plateau (0.29 days yr^{-1}, $p < 0.01$), accounting for 90.39% of SCP anomalies. In contrast, snow onset date (D_o) exhibited unnoticeable changes, explaining 9.58% of SCP changes. Attribution analysis demonstrates that 47.72% of D_e variability stems from increased net shortwave radiation (+0.38 Wm^{-2} yr^{-1}) and rising temperatures (+0.06 °C yr^{-1}) during the melting season, with net shortwave radiation exerting stronger control (R^2 = 0.73) than temperature (R^2 = 0.63). This study establishes the first continuous, high-resolution SCP climatology for the MP, providing mechanistic insights into cryosphere–atmosphere interactions that inform adaptive water resource strategies for climate-vulnerable arid ecosystems in this region.

Keywords: snow cover phenology; Mongolian Plateau; NDSI thresholds; attribution analysis

check for updates

Academic Editor: Hongyi Li

Received: 28 April 2025
Revised: 17 June 2025
Accepted: 26 June 2025
Published: 28 June 2025

Citation: Chen, X.; Lin, S. Rising Net Shortwave Radiation and Land Surface Temperature Drive Snow Cover Phenology Shifts Across the Mongolian Plateau During the 2000–2022 Hydrological Years. *Remote Sens.* **2025**, *17*, 2221. https://doi.org/10.3390/rs17132221

Copyright: © 2025 by the authors. Licensee MDPI, Basel, Switzerland. This article is an open access article distributed under the terms and conditions of the Creative Commons Attribution (CC BY) license (https://creativecommons.org/licenses/by/4.0/).

1. Introduction

As a critical freshwater reservoir, snow cover profoundly influences hydrological cycles, ecosystem stability, and socio-economic systems across the Mongolian Plateau (MP). Firstly, snowmelt serves as a primary recharge source for surface water and groundwater systems, sustaining the MP's hydrological balance [1,2]. This meltwater also regulates soil moisture availability, directly controlling vegetation phenology and productivity [3,4]. The MP spans approximately 515 million acres of rangeland, accounting for 12% of the total rangeland area in Asia. Herding serves as the primary income source in this region, relying on grassland natural resources [5], which are significantly influenced by snow cover dynamics [6]. Moreover, snowpack duration modulates microbial activity and nutrient cycling, indirectly shaping ecosystem resilience. Secondly, the high albedo of

snow cover significantly alters surface energy budgets by reflecting solar radiation, which suppresses land surface temperatures and mitigates soil evaporation [7,8]. This negative feedback mechanism helps stabilize regional climate patterns, particularly during early spring transitions. Thirdly, while beneficial, snow variability also poses hazards. Rapid spring snowmelt frequently triggers floods that disrupt agriculture, pastoralism, and infrastructure [9]. Concurrently, extreme snowfall events exacerbate livestock mortality and humanitarian crises [10]. According to Tachiiri et al. [11], the livestock mortality was closely related with high December snow water equivalent in the preceding year. Given its dual role as a resource and a risk factor, systematic monitoring of spatiotemporal snow dynamics is imperative for advancing climate adaptation strategies, optimizing water resource management, and safeguarding ecological integrity on the MP.

The intensifying scientific interest in snow cover variability and attribution stems from its critical role in climate change assessments, particularly in water-stressed arid and semi-arid regions. Snow cover phenology (SCP), comprising snow onset date (D_o), snow end date (D_e), and snow duration days (D_d), has emerged as a sensitive proxy for tracking seasonal snow dynamics and long-term climatic shifts in the past few decades [1,12]. Utilizing satellite-derived snow cover datasets, published research has documented pronounced SCP changes globally and regionally, including a marked shortened D_d [13–15], an earlier snowmelt onset date [16], an advanced D_e [14,15], and noteworthy shifts in D_o [13,15]. However, most hemispheric-scale SCP studies rely on satellite data with coarse spatial resolutions (5–25 km) and low temporal resolution, introducing significant uncertainty in SCP parameter identification. For instance, key input datasets include a weekly product at 24 km resolution [13] and an 8-day composite at 5 km resolution [14]. This inherent data limitation makes regional-scale SCP information both scarce and highly uncertain. In addition, due to the shortage of high-quality fine-resolution snow cover datasets, critical knowledge gaps persist regarding the MP-specific SCP patterns and their mechanistic responses to rapid climate warming. In addition, while multi-scale analyses identify temperature, precipitation anomalies, and radiative forcing as primary SCP drivers [13,17–21], the relative contributions of these factors remain unresolved for the MP. The conflicting driver effects observed across hemispheric versus local studies require more in-depth exploration of SCP in this climate-sensitive region.

Recent studies have documented substantial climatic transformations across the MP, characterized by pronounced temperature fluctuations and precipitation regime shifts during recent decades [22–24]. These environmental changes pose significant impacts on the spatiotemporal dynamics of SCP in the region. Considering the significance of SCP and the pressing need for comprehensive understanding of snow cover responses to climate change, it is crucial to quantify and understand the spatial and temporal anomalies of SCP and identify the driving forces behind them.

Therefore, the aim of this study is to explore the distribution patterns of SCP and determine its influencing factors in the MP, against the backdrop of rapid climate change. To accomplish this goal, we first extracted the key SCP parameters from the latest version of the daily cloud-gap-filled Moderate Resolution Imaging Spectroradiometer (MODIS) snow cover dataset, covering the 2000–2022 hydrological years (from September 2000 to August 2023). Subsequent spatiotemporal analysis employed time-series decomposition and trend detection algorithms to characterize SCP patterns across elevational and ecological gradients. Finally, we implemented a ridge regression framework incorporating four primary climatic covariates including temperature, precipitation, snow depth, and net shortwave radiation. This multivariate approach effectively addresses multicollinearity while quantifying relative driver contributions to observed SCP variations.

2. Materials and Methods

2.1. Study Area

The MP represents one of Earth's largest contiguous dryland systems, strategically positioned at the intersection of three major atmospheric circulations: the winter Siberian–Mongolian High, East Asian Summer Monsoon, and mid-latitude westerlies, which exhibits exceptional climate sensitivity and ranks among Asia's most vulnerable terrestrial ecosystems. The location of the MP is displayed in Figure 1, which encompasses the entirety of Mongolia, the Inner Mongolia Autonomous Region of China, and south of Russia. The altitude of the MP varies dramatically from 31 to 4176 m, featuring mountainous terrain in the northwest, expansive steppes and rolling hills in the east and center, and Gobi deserts in the south. To focus on the SCP changes in this region, this study confined the study area to stable seasonal snow-covered regions; temporary snow cover in low latitudes and permanent snow cover in high altitudes are excluded in this study.

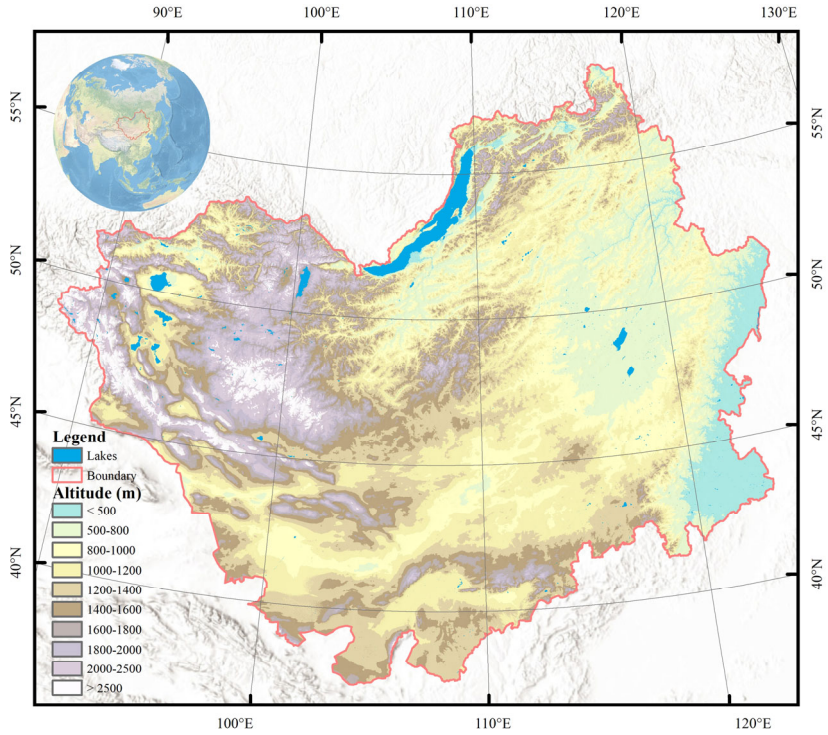


Figure 1. Location of the Mongolian Plateau.

2.2. Dataset

2.2.1. MODIS Snow Cover Dataset

Satellite remote sensing has revolutionized snow cover monitoring since the 1970s, with MODIS emerging as the preeminent sensor for SCP analysis due to its unique combination of daily temporal resolution (500 m nominal spatial resolution) and continuous operation since 2000 [14,25]. This study employs the latest MODIS daily cloud-gap-filled (CGF) snow cover product (MOD10A1F), which addresses the critical limitations of earlier versions through advanced spectral unmixing and a temporal interpolation algorithm [26].

The MODIS snow detection algorithm capitalizes on the distinct spectral signature of snow cover: high visible reflectance coupled with strong near-infrared absorption. These properties enable calculation of the Normalized Difference Snow Index (NDSI), with NDSI $\geq$ 0.4 traditionally indicating snow presence [27]. MOD10A1F introduces three critical advancements: (1) pixels with NDSI < 0.1 are excluded to mitigate false positives from low-reflectance surfaces; (2) continuous NDSI values (0–100 scale) replace binary

classification, enabling probabilistic snow cover estimation; (3) a backward-looking 7-day window replaces cloud-obscured pixels with the most recent valid observation [28]. Compared to legacy versions, the updated MOD10A1F product introduces a gap-filled daily NDSI snow cover layer (CGF_NDSI_Snow_Cover). This layer mitigates cloud obstruction by replacing cloudy pixels with temporally proximate cloud-free observations. Where temporal interpolation is unavailable, spatial filtering of adjacent pixels provides snow cover estimates for these regions [28]. This multi-layered approach reduces cloud-induced data gaps from >30% in standard MODIS products to <10% in MOD10A1F while maintaining 89–92% validation accuracy against ground stations [15,29]. In this study, we adopted the conservative 0.1 NDSI threshold to minimize seasonal snow misclassification in arid environments [30].

2.2.2. Temperature, Precipitation, and Snow Depth Datasets

SCP dynamics are governed by complex cryosphere–atmosphere interactions, with cold-season thermal regimes (temperature), hydrometeorological inputs (precipitation amount), and snowpack evolution (snow depth anomalies) identified as dominant controls [14,17,19]. To quantify these relationships, we utilized 2 m air temperature (monthly mean, °C), total precipitation (monthly cumulative, mm), and snow depth (daily mean, snow water equivalent, mm) from the European Center for Medium-Range Weather Forecasts (ECMWF) Reanalysis v5-Land (ERA5-Land), https://www.ecmwf.int/en/forecasts/dataset/ecmwf-reanalysis-v5-land (accessed on 25 June 2025).

ERA5-Land constitutes a state-of-the-art land surface reanalysis integrating advanced data assimilation with the Hydrology Tiled ECMWF Scheme for Surface Exchanges over Land (HTESSEL) model [31]. ERA5-Land is widely considered suitable for ground-level applications, which provides a superior accuracy in simulating surface air temperature and precipitation across the MP, in comparison to other reanalysis products [32,33]. Furthermore, the snow depth retrievals from ERA-Interim align more closely with in situ observations compared to passive microwave (AMSR-E/AMSR2) and other reanalysis datasets through a hybrid assimilation framework [34]. Compared to its predecessor ERA-Interim, ERA5-Land's enhanced capabilities stem from spatiotemporal resolution (from 0.75° to 0.10°), observation integration, and snow density parameterization. This combination of high-resolution forcing and validated land surface representation makes it particularly suited for diagnosing SCP–climate linkages in heterogeneous dryland environments.

2.2.3. Solar Radiation Dataset

Emerging evidence highlights surface radiative flux as a critical yet underexplored driver of snow cover anomalies, operating through snow–albedo feedback loops that amplify cryosphere changes [1,21]. This self-reinforcing mechanism initiates when increased surface net shortwave radiation (SNSW) accelerates snowmelt, subsequently reducing surface albedo by 40–60% as snow-covered terrain transitions to bare ground or vegetation [35]. The absorbed radiative surplus drives localized warming of 1.5–3.0 °C per snow cover loss decade at high latitudes, accounting for 46.2 ± 5.8% of Northern Hemisphere (NH) cryosphere retreat in the sixth phase of the Coupled Model Intercomparison Project (CMIP6) projections [36]. To investigate the potential connection between surface radiation and SCP, we incorporated monthly surface net shortwave flux from the Clouds and the Earth's Radiant Energy System (CERES) Energy Balanced and Filled (EBAF) dataset [37] in the attribution analysis, where net shortwave flux is defined as the difference between downward and upward shortwave fluxes. The CERES-EBAF product demonstrates superior accuracy over comparable gridded radiation budget datasets [38], establishing it as the predominant reference standard in radiative flux validation. This status derives from its

rigorous energy balance closure framework, decadal-scale stability, and regionally verified performance metrics [39].

2.2.4. Data Preparation

To maintain dimensional consistency across diverse datasets used in the attribution analysis, all input variables were standardized to a uniform 0.10° geographic grid utilizing the gdalwarp utility. The choice of resampling method was determined by the resolution of the data to prioritize geophysical integrity: For high-resolution SCP parameters derived from MOD10A1F, the "average" method was employed during resampling. This method computes the mean of all contributing non-NODATA pixels. For variables from ERA5-Land, the "nearest-neighbor" method was selected, as it retains the inherent land–atmosphere coupling present in HTESSEL model outputs. For surface net shortwave radiation data from the CERES, the "Cubic spline interpolation" method was chosen, which refines coarse-resolution radiative fluxes while ensuring energy balance conservation.

In accordance with the cryospheric hydrological cycles in northern Eurasia [40], this study adopted a hydrological year framework in the SCP derivation. The hydrological year (t) is delineated from September of the previous year (t1) to August of the current year (t). Within this framework, the accumulation season is identified as September to December of the previous year ($t-1$), while the melting season is pinpointed as March to June of the preceding year (t1). To attribute changes in D_o and D_e, we derived seasonal composites by averaging 2 m air temperature, total precipitation, snow depth, and net shortwave radiation separately for accumulation (September–December) and melting seasons (March–June). This temporal partitioning enhances attribution robustness by isolating climate variable influences during critical phenological phases.

2.3. Methods

The flowchart of this study is illustrated in Figure 2. Firstly, the snow cover was identified using NDSI thresholds of 0.1. The value of 0.1 represents the minimum NDSI value of MOD10A1F V6. Secondly, the SCP retrieval process over the MP was carried out. Thirdly, changes in SCP were attributed to various climate variables, such as land surface temperature, precipitation, snow depth, and net shortwave radiation.

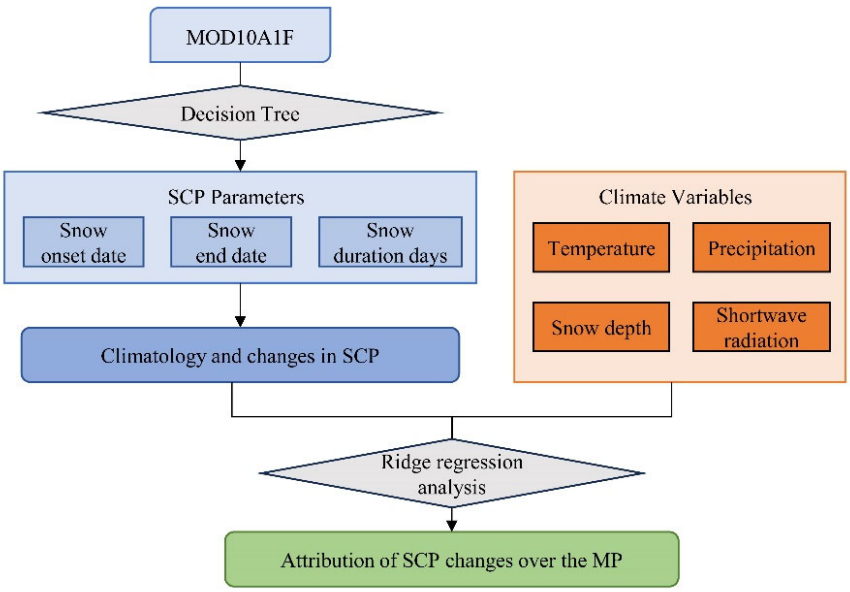


Figure 2. Flowchart of this study.

2.3.1. SCP Parameter Detection

The SCP parameters were extracted utilizing the MOD10A1F via a decision trees methodology. For a given grid cell, D_o was designated as the date of the initial five consecutive images exhibiting an NDSI $\geq$ 0.1, while D_e was allocated as the date of the terminal five consecutive images with an NDSI < 0.1. Furthermore, D_d represents the days elapsed between D_o and D_e. This methodology mitigates the impact of transient snow cover on the SCP retrieval, ensuring that persistent snow is consistently captured for analysis. To scrutinize the climatology and dynamic evolution of long-term SCP across the MP, this study concentrated on areas characterized by stable snow cover, defined as regions where $D_d \geq 30$ days.

2.3.2. Attribution Analysis Method

Given the direct thermodynamic coupling between D_d and its phenological endpoints D_o and D_e, this study primarily focuses on identifying dominant controls over D_o and D_e. The influences of four climatic drivers (2 m air temperature, total precipitation, snow depth, and net shortwave radiation) on SCP were meticulously examined using ridge regression analysis. Ridge regression analysis effectively mitigates collinearity among covarying climatic drivers of SCP via L2-norm regularization. By penalizing coefficient magnitudes, this approach reduces inflation and instability caused by multicollinearity—a methodology successfully applied in SCP attribution studies, as demonstrated by Chen et al. [18] and Peng et al. [19].

Firstly, the drivers were normalized to facilitate cross-comparison of variables with disparate units and magnitudes. Normalizing predictors enables the evaluation of their influence without being skewed by their respective magnitudes, thereby ensuring a more robust regression analysis. For a given variable X_i, its z-score (X_{iz}) was computed using Equation (1) as per [41]:

$$X_{iz} = \frac{X_i - \mu_X}{\delta_X} \quad (1)$$

where μ_x represents the average value of the variable X_i, while δ_x denotes the standard deviation of the same variable X_i.

Secondly, a ridge regression analysis was conducted to evaluate the sensitivity of D_o and D_e to the four presumed drivers using Equations (2) and (3). The hypothesis is that the interannual variability of D_o is governed by the competing influences of accumulation-season averaged 2 m temperature (T_a), total precipitation (P_a), and net shortwave radiation (SW_a). To attribute changes in D_o, a regression was performed with D_o serving as the dependent variable and T_a, P_a, and SW_a acting as independent variables using Equation (2):

$$D_o = \beta_1 \times T_a + \beta_2 \times P_a + \beta_3 \times SW_a + \varepsilon_1 \quad (2)$$

Here, β_1, β_2, and β_3 are the regression coefficients for T_a, P_a, and SW_a, while ε_1 is the residual. Therefore, the impact of T_a, P_a, and SW_a on D_o anomalies is captured by the terms $\beta_1 \times T_a$, $\beta_2 \times P_a$, and $\beta_3 \times SW_a$, respectively. To determine the contributions of T_a, P_a, and SW_a to D_o, we regressed the annual time series of D_o z-scores against the corresponding time series of T_a, P_a, and SW_a z-scores. Then, the regression coefficients β_1, β_2, and β_3 were applied to the T_a, P_a, and SW_a z-scores to compute their contributions to the D_o z-scores.

Additionally, D_e is affected by the accumulation-season averaged snow depth (SD_a) and the melting-season averaged 2 m air temperature (T_m) and net shortwave radiation (SW_m). Consequently, we hypothesized that the interannual variability of D_e is influenced

by T_m, SD_a, and SW_m. In our analysis, we employed Equation (3) to regress D_e as the dependent variable against the independent variables T_m, SD_a, and SW_m.

$$D_e = \beta_4 \times T_m + \beta_5 \times SD_a + \beta_6 \times SW_m + \varepsilon_2 \quad (3)$$

Here, β_4, β_5, and β_6 are the regression coefficients for T_m, SD_a, and SW_m, while ε_2 is the residual. The contributions of T_m, SD_a, and SW_m to D_e anomalies are reflected by the terms $\beta_4 \times T_m$, $\beta_5 \times SD_a$, and $\beta_6 \times SW_m$, respectively. Similarly, the contributions of T_m, SD_a, and SW_m to D_e were ascertained by regressing the z-scores of D_e against the z-scores of T_m, SD_a, and SW_m. Subsequently, the derived regression coefficients were multiplied by the corresponding z-scores of T_m, SD_a, and SW_m to infer their individual contributions to the D_e z-scores.

3. Results

To systematically investigate the SCP dynamics across the MP during the 2000–2022 hydrological years, we first extracted the key SCP parameters, including D_o, D_e, and D_d, from the MOD10A1F using a decision tree approach. Then, we analyzed the climatology and spatiotemporal trend of SCP. Finally, we conducted multivariate attribution modeling to diagnose the underlaying drivers of SCP during this corresponding period.

3.1. Climatology of SCP

To investigate the spatial distribution of SCP across the MP, 23-year averages of D_o, D_e, and D_d were computed spanning the hydrological years from 2000 to 2022. These spatial distributions of the mean values are depicted in Figure 3.

As shown in Figure 3, the SCP across the MP is characterized by pronounced spatial heterogeneity, driven by the interactive effects of latitude, topography, and elevation. The spatial patterns of D_o, D_e, and D_d exhibit a clear latitudinal gradient from south to north, with additional modulation by mountainous terrain. Thermal gradients across the MP act as the primary driver of SCP dynamics. High-latitude areas surrounding Lake Baikal, together with elevated regions such as the Sayan Mountains, northern Hangai Mountains, western Altai Mountains, and northeastern Kalar Mountains, exhibit an earlier D_o due to lower mean annual temperatures. For example, the Sayan Mountains (average elevation > 2000 m) experience D_o in early October, nearly 4–6 weeks earlier than the southern MP plains (e.g., Gobi–Altai Plateau) where D_o typically occurs in late November. Conversely, low-elevation zones in the southern MP, influenced by the Siberian high-pressure system and continental aridity, show delayed D_o and earlier D_e, resulting in a truncated snow season. Moreover, the spatial distribution of D_e (Figure 3b) demonstrates a significant inverse correlation with D_o, a pattern supported by statistical analysis: regions with an earlier D_o exhibit a later D_e, reflecting a compensatory mechanism in SCP. This relationship implies that areas with prolonged snow cover (e.g., northern MP) maintain snow until late April to early May, whereas southern regions experience snowmelt by mid-March. Consequently, D_d shows a strong latitudinal gradient, with high-latitude/high-altitude zones exceeding 180 days (e.g., Altai Mountains) and southern plateaus averaging < 90 days (Figure 3c).

Comparative analysis with the NH SCP matrices reported by Chen et al. [14] revealed significant regional disparities. The MP exhibited a distinctive SCP pattern, characterized by a delayed D_o, an earlier D_e, and a truncated D_d relative to the hemispheric average. This divergence in SCP dynamics highlights the MP's unique climatological and topographical influences on snow cover processes, which are likely mediated by factors such as local temperature gradients, elevation, and atmospheric circulation patterns. These differences can be attributed to the unique geographical location and climate regime of the MP. The MP

is situated in a continental climate zone, which experiences strong seasonal temperature fluctuations. The lack of moderating effects from large water bodies, as compared to coastal regions in the NH, leads to more extreme temperature changes. In winter, cold air masses can rapidly cool the surface, but the relatively dry atmosphere may also result in less snowfall and a later onset of significant snow cover. In spring, the continental climate warms quickly, causing an earlier melting of the snowpack and a shorter overall D_d. In addition, different with previous studies by Chen et al. [14] and Choi et al. [13] focusing on broad-scale SCP dynamics, the present study leverages high-resolution datasets to offer a granular examination of SCP variability across the MP. This enhanced spatial resolution enables a more nuanced understanding of the intricate relationships between climate change, topography, and snow hydrology, which are conducive to more accurate hydrological modeling and climate change impact assessments in the MP.

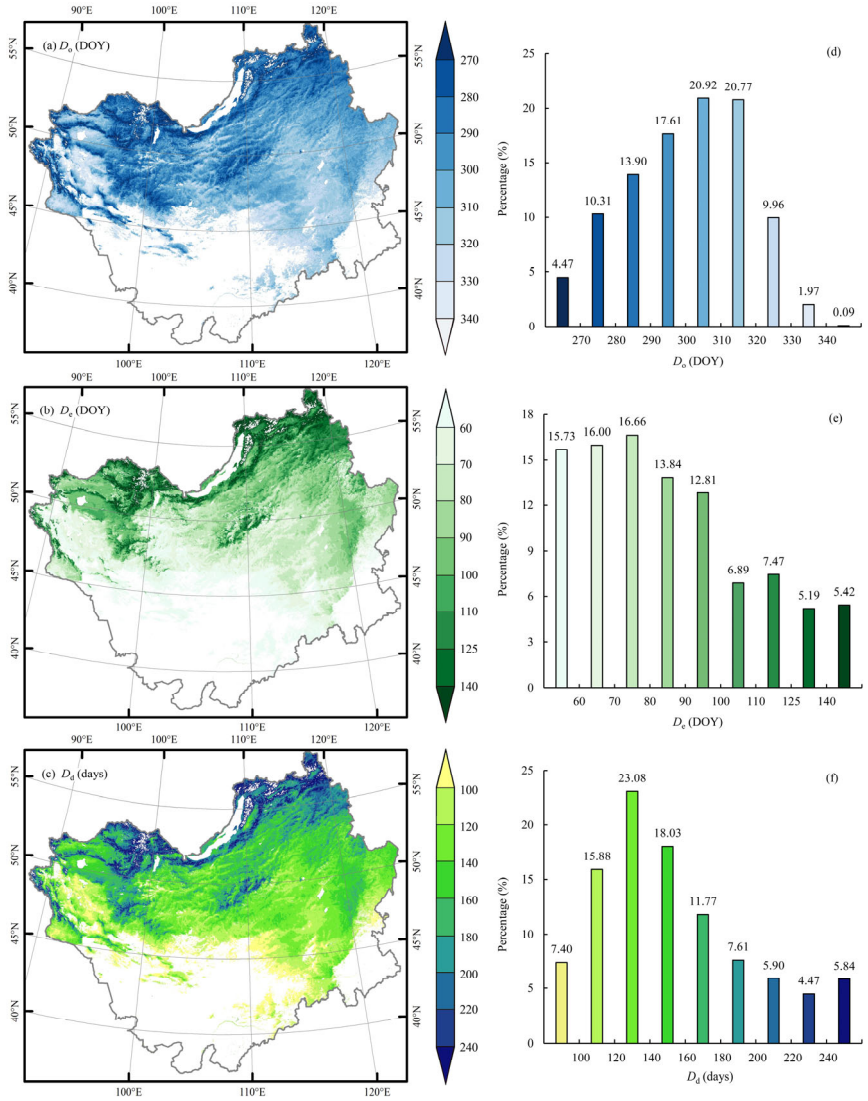


Figure 3. Spatial distribution of 23-year mean values for (**a**) snow onset date (D_o), (**b**) snow end date (D_e), and (**c**) snow duration days (D_d) across the Mongolian Plateau during 2000–2022 hydrological years; (**d**–**f**) histogram distributions of (**d**) D_o, (**e**) D_e, and (**f**) D_d over the same period.

3.2. Changes in SCP

3.2.1. Spatial Variation

Figure 4 illustrates the spatial distribution of the trends in D_o, D_e, and D_d across the MP during the 2000–2022 hydrological years. In this analysis, the magnitude of change for

each parameter was quantified by multiplying the estimated linear slope of the trend by the time interval spanning the study period.

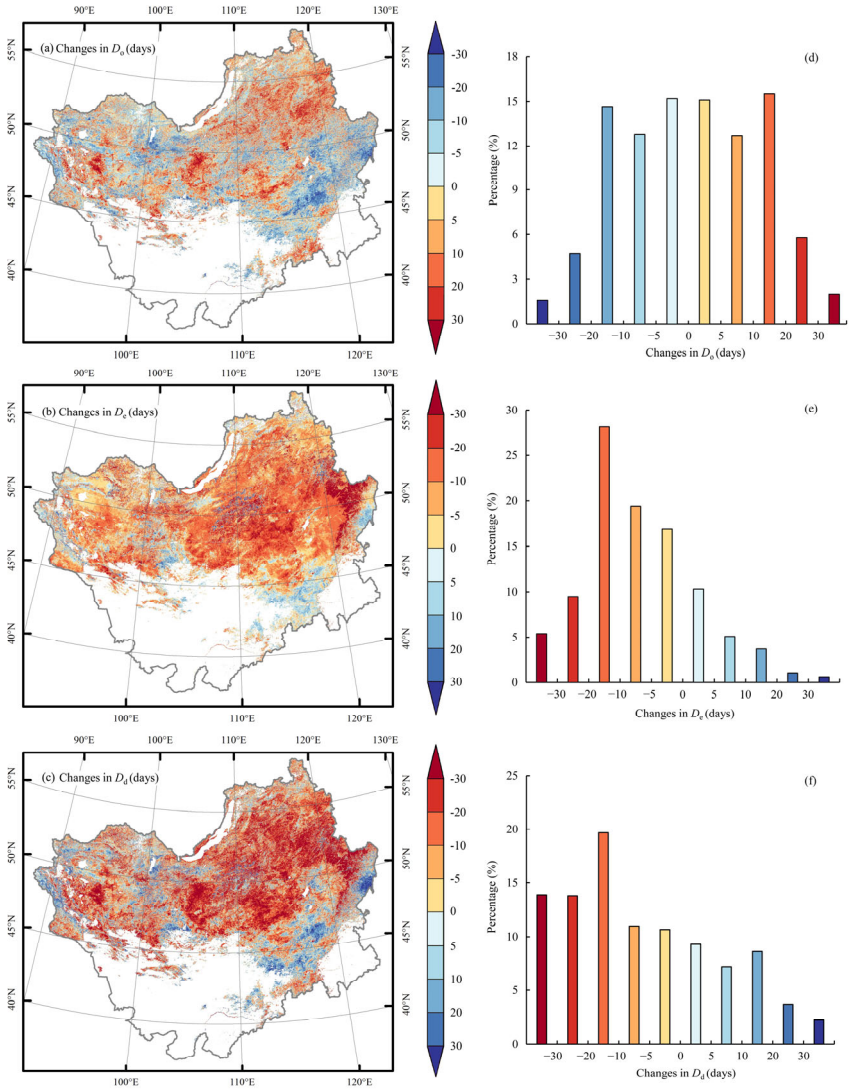


Figure 4. Changes in (**a**) snow onset date (D_o), (**b**) snow end date (D_e), and (**c**) snow duration days (D_d) across the Mongolian Plateau during 2000–2022 hydrological years; (**d**–**f**) histograms of trend magnitudes for (**d**) D_o, (**e**) D_e, and (**f**) D_d over the same period.

During the hydrological years from 2000 to 2022, significant spatial heterogeneity was observed in the trends in D_o across the MP, as shown in Figure 4a. Spatially, the changes in D_o were inconsistent. In the northeastern region of Inner Mongolia, D_o showed a notable advance, whereas in the northeastern part of Mongolia, a substantial delay was detected. Histogram analysis (Figure 4d) reveals that pixels with advanced and delayed D_o accounted for 48.92% and 51.08% of the D_o anomalies during this period, indicating a nearly balanced spatial distribution of opposite trends. In contrast to D_o, D_e exhibited a widespread and significant advance across the MP throughout the study period. The most pronounced advancement in D_e occurred in the eastern MP around 50°N, while slight delays were observed at the southern edge of the stable snow area in the MP (Figure 4b). As shown in the histogram (Figure 4e), 79.27% of the pixels on the MP displayed an advancing trend in D_e, with the largest proportion (36.25%) comprising pixels where D_e advanced by 0−10 days (negative values denote earlier occurrence). In contrast, only a small fraction of pixels (15.37%) showed a delayed trend in D_e, highlighting the dominance of early-

ending patterns for the hydrological period 2000−2022 across most of the plateau. In addition, as illustrated in Figure 4c,f, the combined effect of anomalies in D_o and D_e led to a reduction in D_d across the MP in this period. Histogram analysis shows that 69.03% of grid cells in the study area exhibited shortened D_d during this period, highlighting a dominant trend toward shorter snow cover durations. In contrast, regions with lengthened D_d accounted for approximately 30.99% of the study area, indicating a minority but still notable countertrend.

3.2.2. Temporal Variation

The temporal variations in SCP changes across the MP during the 2000–2022 hydrological years are illustrated in Figure 5. The trend in D_o, D_e, and D_d over the MP during this period was estimated to be -0.03 days yr^{-1} ($p > 0.05$), -0.29 days yr^{-1} ($p < 0.0$), and -0.26 days yr^{-1} ($p > 0.0$), respectively, which suggests a statistically insignificant advance in D_o, a significant forward in D_e, and a marked shortening of D_d in this specific period. This temporal variation in D_o across the MP is consistent with the reported noteworthy shifts in D_o over the NH [13,14] and high-mountain Asia [15] in the similar period. Meanwhile, the forward speed of D_e on the MP is greater than the average value in the NH (-1.12 days decade^{-1}, $p < 0.05$) [14], but less than that in high-mountain Asia (-1.69 days yr^{-1}) [15] within a similar time interval.

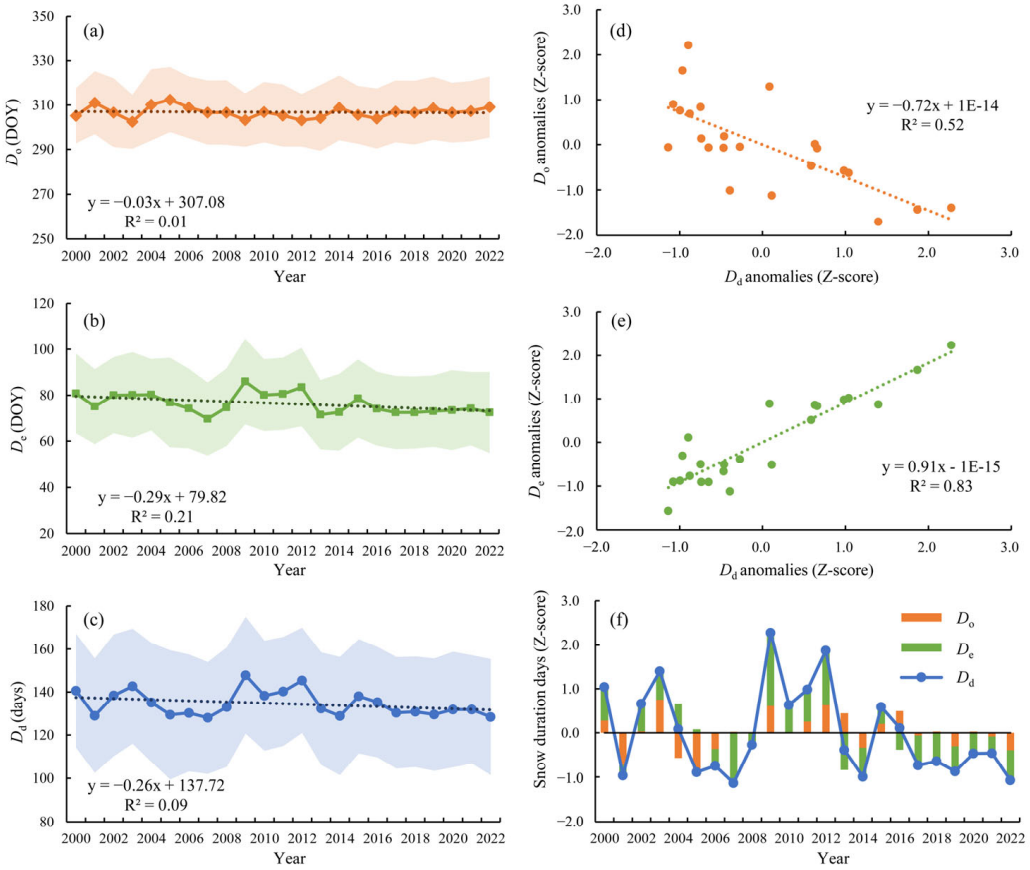


Figure 5. The 23-year variation in (**a**) snow onset date (D_o), (**b**) snow end date (D_e), and (**c**) snow duration days (D_d) across the Mongolian Plateau during 2000–2022 hydrological years; (**d**,**e**) linear correlation analyses between (**d**) D_o and D_d, (**e**) D_e and D_d over the same period; (**f**) contributions of D_o and D_e to D_d.

A detailed exploration is conducted to clarify the inter-relationships between D_o, D_e, and D_d. Pearson correlation analysis reveals a high correlation between D_e and D_d

(R^2 = 0.83, $p < 0.05$), with a moderate yet statistically significant correlation between D_o and D_d (R^2 = 0.52, $p < 0.05$). Variance decomposition analysis further demonstrates that temporal changes in D_o account for 9.58% of the observed variability in D_d, whereas changes in D_e explain 90.39% of this variability. Given the statistically insignificant trend in D_o (-0.03 days yr^{-1}, $p > 0.05$), we conclude that the recent decadal shortening of D_d (-0.26 days yr^{-1}, $p < 0.05$) is predominantly driven by the advancing trend in D_e (-0.29 days yr^{-1}, $p < 0.05$).

3.3. Attribution Analysis

3.3.1. Attribution Analysis of Changes in D_o

To determine the key factors influencing D_o anomalies over the MP, a sensitivity analysis was conducted using Equation (2), as shown in Figure 6. The spatial distributions of the 23-year mean T_a, P_a, and SW_a over the MP during the 2000–2022 hydrological years are presented in Figure 6a–c. Influenced by solar radiation, both T_a (Figure 6a) and SW_a (Figure 6c) exhibit a distinct decreasing trend from the southern to the northern part of the MP. Significantly, this pattern stands in stark contrast to the distribution of P_a (Figure 6b), which reveals an increasing trend from south to north across the MP.

Changes in T_a, P_a, and SW_a, along with the sensitivities of D_o to variations in T_a, $P_a$and SW_a, are displayed in Figure 6d–f. A 23-year linear trend analysis shows that most grid cells in the snow-covered areas of the MP exhibit a significant warming trend in T_a (Figure 6d), with the most pronounced warming occurring in the northeastern region and sporadic cooling observed in the northwestern region. He et al. [42] analyzed data from 16 meteorological stations in the typical grassland areas of the MP from 1978–2020 and found an overall warming trend, consistent with our findings on the spatial pattern of temperature change. Meanwhile, SW_a increases in southern areas but decreases in both eastern and western regions (Figure 6f). The warming of the MP and the increase in net radiation are inherently linked to phase transitions of the Pacific Decadal Oscillation (IPO) and Atlantic Multidecadal Oscillation (AMO). Cai et al. [43] revealed that the combined phase changes in IPO and AMO since the late 1980s have triggered a mid-latitude atmospheric teleconnection wave train, inducing an anticyclonic circulation tendency over the MP. This enhances downward solar radiation and land–atmosphere feedback in the region, driving the observed warming phenomenon [43]. Concurrently, the P_a over the MP shows an overall decreasing trend during the 2000–2022 hydrological years (Figure 6e), with notable exceptions in regions such as the Greater Khingan Mountains in northeastern China and Russia's Yablonovy Mountains, which exhibit increasing precipitation trends [42]. This finding is consistent with station-based analysis results, which suggest that winter precipitation on the MP has significantly increased in recent years [44].

The sensitivities of D_o to variations in T_a, P_a, and SW_a are displayed in Figure 6g–i. The sensitivity analysis derived from Equation (3) demonstrates a positive correlation between D_o and T_a across the MP during the 2000–2022 hydrological years, with a sensitivity coefficient of 0.17 ($\pm$0.21) days $^{\circ}$C^{-1} (Figure 6g). This indicates that a 1 $^{\circ}$C increase in T_a delays D_o by 0.17 ($\pm$0.21) days. In contrast, a negative correlation exists between D_o and P_a, with a sensitivity of -0.22 ($\pm$0.21) days mm^{-1}, meaning a 1 cm increase in P_a advances D_o by 0.48 ($\pm$0.18) days (Figure 6h). Notably, the sensitivity of D_o to SW_a is the most pronounced among the three variables, at 0.33 ($\pm$0.27) days per Wm^{-2}, signifying that a 1 Wm^{-2} increase in SW_a accelerates D_o advance by 0.33 ($\pm$0.27) days (Figure 6i).

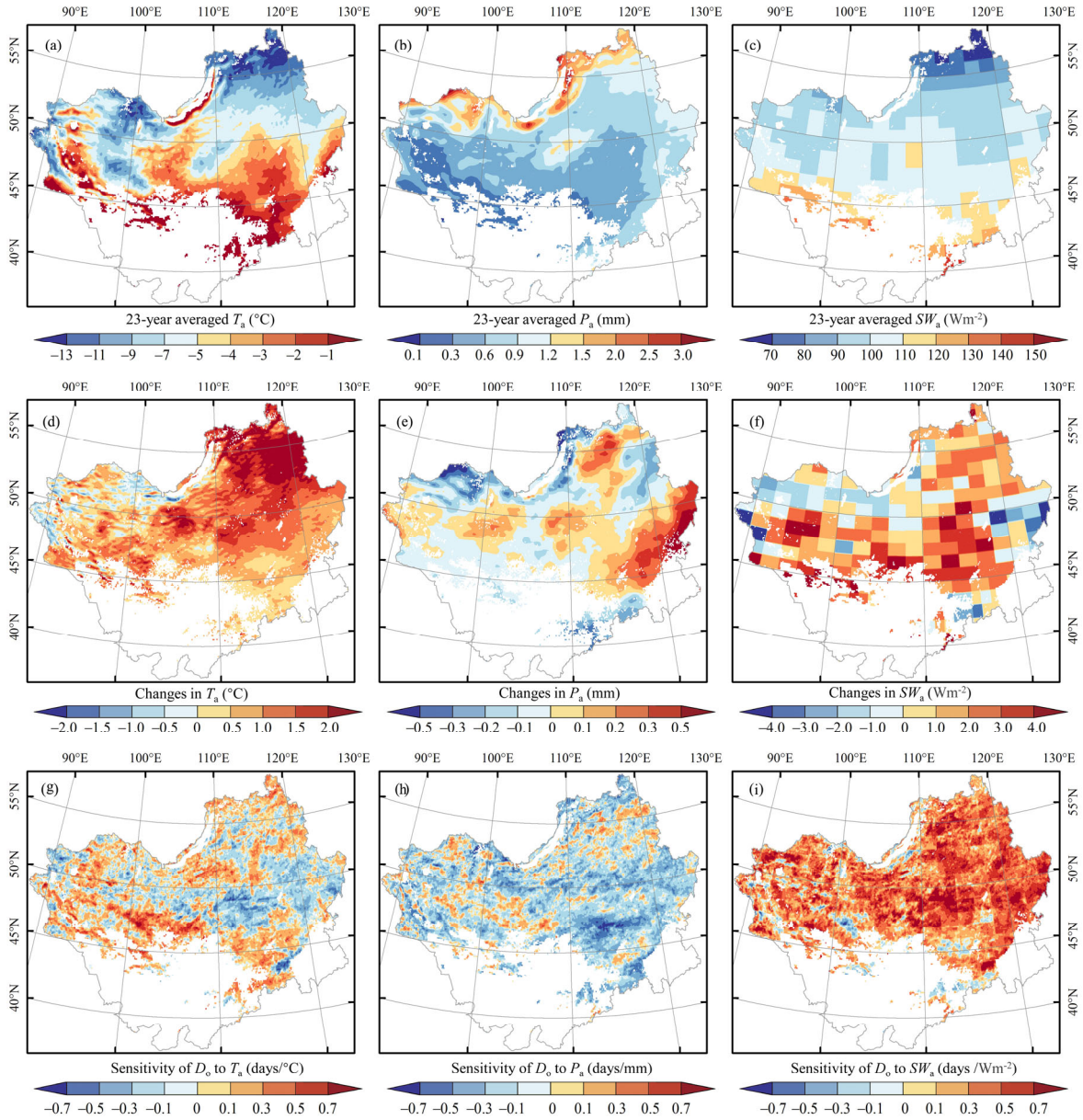


Figure 6. Spatial distributions of 23-year mean accumulation-season (**a**) temperature (T_a), (**b**) precipitation (P_a), and (**c**) net shortwave radiation (SW_a) across the Mongolian Plateau (MP) during 2000–2022 hydrological years; (**d**–**f**) 23-year trends in T_a, P_a, and SW_a, respectively; (**g**–**i**) sensitivity of D_o to variations in T_a, P_a, and SW_a across the MP.

The attribution analysis of D_o across the MP during the 2000–2022 hydrological years is presented in Figure 7. Temporal variation analysis shows that T_a, P_a, and SW_a displayed no significant trends on the MP over this period. However, linear correlation analysis revealed that anomalies in D_o anomalies were statistically correlated with T_a ($R^2 = 0.23$, $p < 0.05$) and SW_a ($R^2 = 0.42$, $p < 0.05$), though the correlation with P_a ($R^2 = 0.16$, $p > 0.05$) was not significant. Contribution analysis further indicates that SW_a contributed 61.07% to D_o anomalies, followed by P_a (31.27%) and T_a (0.49%). This predominance arises because radiative flux provides direct phase-change energy to the snowpack, whereas ambient air warming alone drives inefficient melting. Heat transfer via conduction/convection—mediated by turbulent energy fluxes—constitutes an indirect and thermodynamically slower pathway [45,46]. Thus, the D_o anomalies on the MP during the 2000–2022 hydrological years were predominantly driven by SW_a changes.

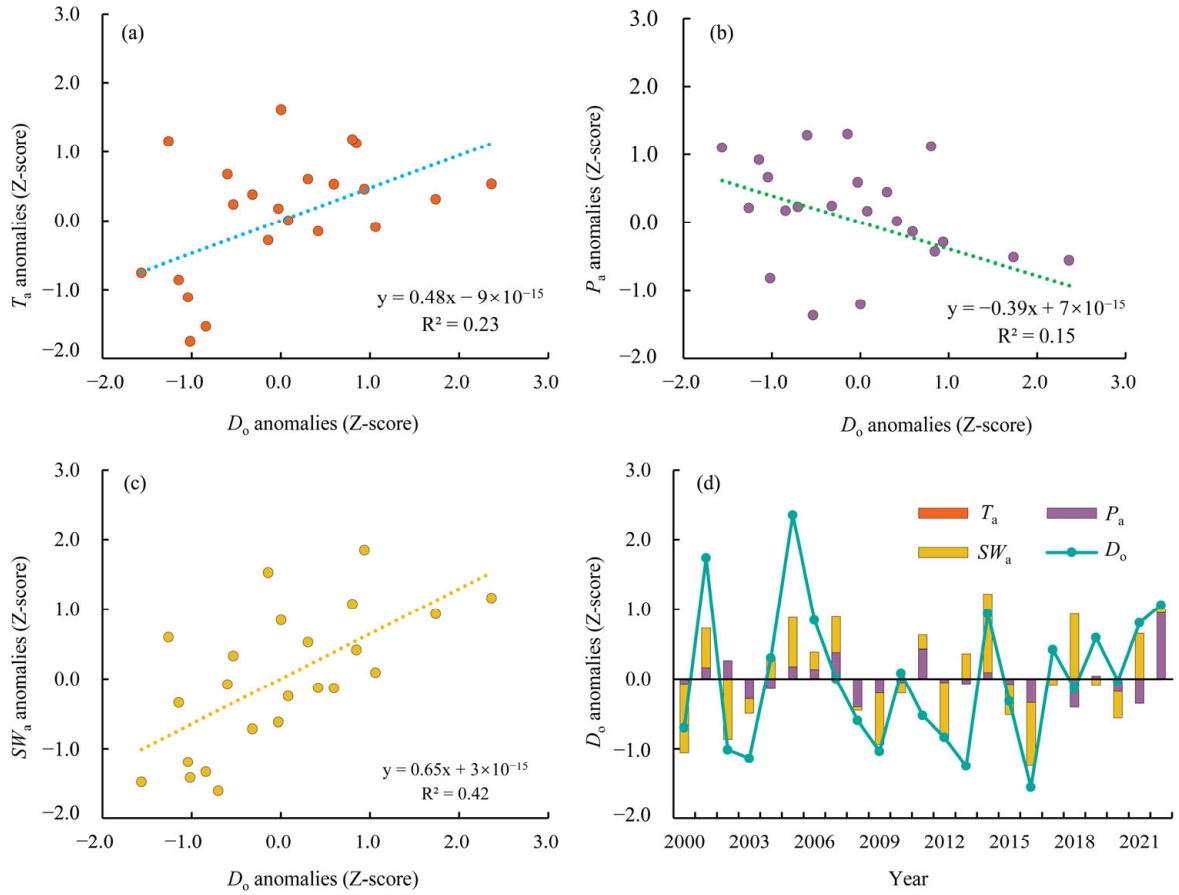


Figure 7. Linear correlations between snow onset date (D_o) and accumulation-season (**a**) temperature (T_a), (**b**) precipitation (P_a), and (**c**) net shortwave radiation (SW_a) across the Mongolian Plateau during 2000–2022 hydrological years; (**d**) contributions of T_a, P_a, and SW_a to D_o changes across the MP over the same period.

3.3.2. Attribution Analysis of Changes in D_e

To identify the dominant drivers of D_e anomalies across the MP during the 2000–2022 hydrological years, a sensitivity analysis was performed using Equation (4), as shown in Figure 8. The spatial distributions of the 23-year mean of T_m, SD_a, and SW_m across the MP in this period are presented in Figure 8a–c. Changes in T_m, SD_a, and SW_m, along with the sensitivity of D_e to variations in these variables, are illustrated in Figures 8d–f and 8g–i, respectively.

Similar to the spatial distribution patterns of T_a and SW_a, the 23-year mean values of T_m (Figure 8a) and SW_m (Figure 8c) exhibit a south-to-north decreasing trend across the MP during the 2000–2022 hydrological years, primarily regulated by solar radiation. In contrast, SD_a shows a south-to-north increasing trend over the same period (Figure 8b). Driven by phase transitions in the IPO and AMO, the 23-year trends (2000–2022) in T_m (Figure 8d) and SW_m (Figure 8f) exhibit significant upward trends across the MP [42,43]. This warming and radiation intensification are closely linked to the combined influence of IPO-/AMO-induced atmospheric teleconnections, which enhance downward solar radiation and land–atmosphere energy feedback over the MP [43]. Concurrently, SD_a has undergone a general decline across the MP, with the most pronounced decreases observed in the northeastern region. Notable exceptions include the Greater Khingan Mountains in the east and the Altai Mountains in the west, where SD_a has remained relatively stable or experienced minor increases, likely due to localized topographic effects on snow accumulation and regional moisture circulation patterns [47].

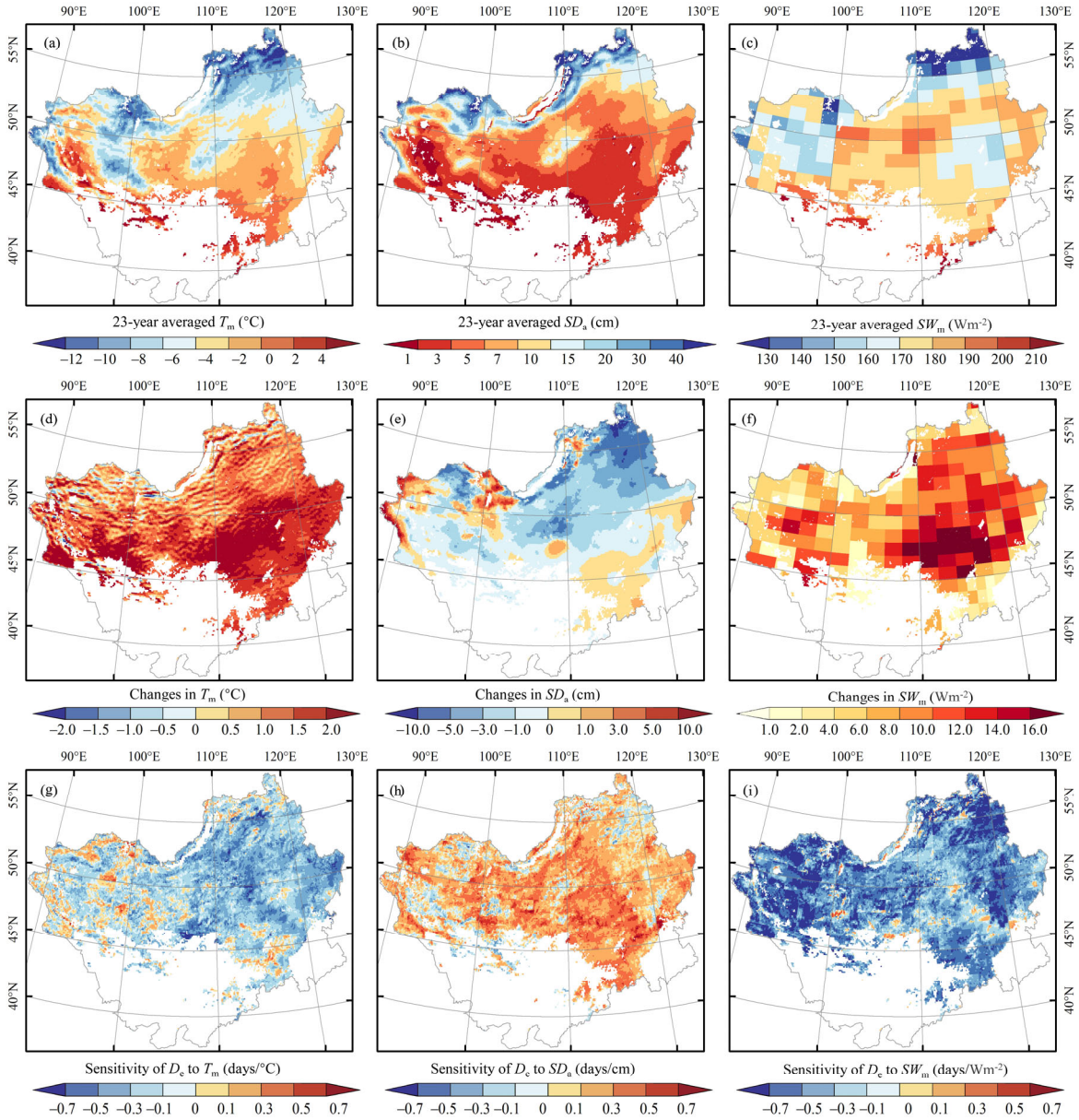


Figure 8. Spatial distributions of 23-year mean (**a**) melting-season temperature (T_m), (**b**) accumulation-season snow depth (SD_a), and (**c**) melting-season net shortwave radiation (SW_m) across the Mongolian Plateau (MP) during 2000–2022 hydrological years; (**d**–**f**) 23-year trends in T_m, SD_a, and SW_m, respectively; (**g**–**i**) sensitivity of D_e to variations in T_m, SD_a, and SW_m across the MP.

The sensitivity analysis based on Equation (4) indicates that D_e exhibits a negative sensitivity of −0.22 (±0.21) days °C^{-1} to T_m, suggesting that a 1 °C increment in T_m would lead to a delay in D_e by 0.17 (±0.21) days (Figure 8g). Meanwhile, the sensitivity of D_e to SD_a is estimated to be 0.17 (±0.19) days cm^{-1}, indicating that a 1 cm increase in SD_a would cause a delay in D_e by 0.17 (±0.19) days (Figure 8h). In comparison, the sensitivity of D_e to SW_m is the highest, registering at −0.48 (±0.25) days per Wm^{-2}, suggesting that a 1 Wm^{-2} rise in SW_m would prompt an advance in D_e by 0.48 (±0.25) days (Figure 8i). Temporal variation analysis reveals that SW_m increased at a rate of 0.38 Wm^{-2} yr^{-1} ($p < 0.05$), while T_m rose at 0.06 °C yr^{-1} ($p < 0.05$) across the MP during the 2000–2022 hydrological years. In contrast, SD_a exhibited no significant trends over the same period. Moreover, a comprehensive contribution analysis demonstrated significant correlations (at the 95% confidence level) between changes in D_e and T_m (Figure 9a), SD_a (Figure 9b), and SW_m (Figure 9c). Consistent with the attribution analysis for D_o, SW_m emerged as

the primary driver of D_e variability, accounting for 47.72% of D_e anomalies. T_m ranked as the second most influential factor, contributing 41.22% to D_e changes, while SD_a had a less pronounced but still notable impact, explaining 22.15% of the variability. Given the lack of significant temporal changes in SD_a over this period, SW_m and T_m dominated the control over D_e anomalies, highlighting its critical role in modulating snowmelt-driven hydrological processes across the MP.

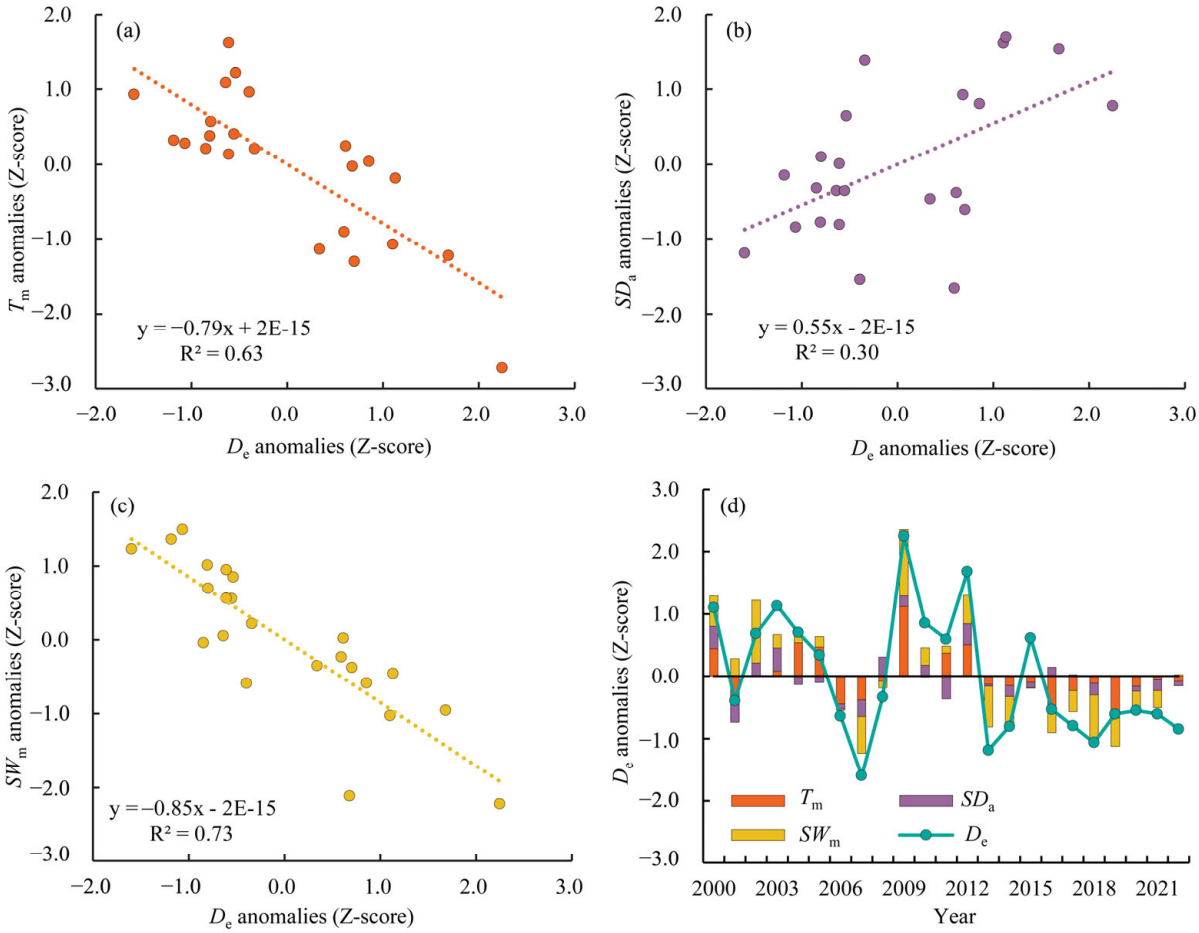


Figure 9. Linear correlations between snow end date (D_e) and (**a**) melting-season temperature (T_m), (**b**) accumulation-season snow depth (SD_a), and (**c**) melting-season net shortwave radiation (SW_m) across the Mongolian Plateau during 2000–2022 hydrological years; (**d**) contributions of T_m, SD_a, and SW_m to D_e changes across the MP over the same period.

Notably, this finding contrasts with prior attribution analyses of D_e in the NH, which predominantly identified T_m as the primary climatic driver of earlier snowmelt across the NH [14]. However, our results align partially with Wang et al. [48], who emphasized that spring snow cover reduction is driven by intraseasonal variability in surface energy fluxes. This discrepancy may stem from the distinct spatial scale and climatic context of the MP, where atmospheric teleconnections (e.g., IPO/AMO phase transitions) and regional radiation patterns exert stronger control over snowmelt dynamics than mean temperature alone. While NH studies often focus on broad temperature trends, our regional analysis reveals that shortwave radiation, as a key component of surface energy balance, plays a dominant role in modulating snowmelt timing and discharge anomalies on the MP.

4. Discussion

Given the MP is one of the largest arid and inland plateaus in East Asia, accurate estimates of SCP are critical for improving atmospheric reanalysis [49], climate predictions [50], and understanding vegetation dynamics [4,51]. Leveraging the latest version of MODIS snow cover products, this study investigates the spatial–temporal distribution and driving mechanisms of SCP across the MP at the highest achievable resolution compared to prior research. The high temporal frequency (daily revisit) and near-complete spatial coverage of MOD10A1F significantly reduce uncertainties in SCP retrievals—challenges commonly associated with low temporal resolution and fragmented coverage in other optical snow products. This advancement is particularly valuable for local climate modeling, ecological monitoring, and hydrological forecasting in the MP, where snow cover exerts profound impacts on energy balance, water resources, and vegetation phenology.

Employing MOD10A1F-derived SCP parameters at refined spatiotemporal resolutions, this study reveals statistically insignificant trends in D_o, significant advancement in D_e, and consequent shortening of D_d across the MP during the hydrological years 2000–2022. These findings partially align with continental-scale SCP studies by Choi et al. [13] and Chen et al. [14], which identified D_e anomalies as the primary driver of SCP changes during 1967–2008 and 2001–2020, respectively. However, these results contrast with Allchin and Déry [52], who attributed NH SCP variations from 1972–2017 primarily to shifting spatiotemporal patterns of D_o. The discrepancy may stem from differences in temporal coverage, as attribution analyses are highly sensitive to the study period selected. For instance, shorter-term trends (e.g., our 23-year dataset) may reflect localized climatic drivers like SW_m intensification, whereas longer-term hemispheric studies emphasize broader teleconnections linked to D_o. This highlights the importance of temporal scale in interpreting snow cover–climate relationships across heterogeneous regions like the MP.

The findings of this study rely on the latest version of MOD10A1F snow cover products and are therefore inherently subject to the limitations of this dataset. MOD10A1F has well-documented imperfections, primarily arising from challenges in cloud–snow discrimination and snow detection under conditions such as low illumination, high solar zenith angles, shadowed surfaces, and complex mountainous terrain [53,54]. These limitations were not addressed in this study and will require advancements in snow detection algorithms, cloud–snow discrimination techniques, and sensor optimization in future research. Nevertheless, within the current technical framework, MOD10A1F remains the most reliable dataset for SCP monitoring across the MP, balancing spatial–temporal resolution and coverage for large-scale hydrological and climatic analyses. Furthermore, our attribution analysis relied on ridge regression, which inherently assumes linear relationships between SCP and climate variables. While this approach mitigates multicollinearity, it may overlook complex non-linear interactions among drivers. Future studies could enhance this by incorporating polynomial features or integrating ridge regression with non-linear transformations to better capture these intricate relationships.

Recent climate projections indicate that a sustained reduction in seasonal snow cover extent is highly likely under continued global warming. This trend is amplified by a positive snow–albedo feedback loop in the Earth's climate system, where declining snow cover reduces surface reflectivity and enhances land–atmosphere energy absorption. Consequently, future research must deepen our understanding of how SCP will respond to projected warming, particularly in regions like the MP that are highly sensitive to climate change. Additionally, snow cover fluctuations exert profound impacts on natural vegetation phenology, especially in grassland and forest ecosystems. To address these complexities, future studies should employ integrated approaches that link snow cover dynamics, vegetation phenology, and climate models, enabling a more holistic understanding

of biophysical interactions under escalating global temperatures. Such research is critical for improving ecosystem vulnerability assessments and adaptive management strategies in snow-dominated regions.

5. Conclusions

This study analyzed the spatial–temporal distribution, trends, and driving forces of SCP across the MP during the 2000–2022 hydrological years, leveraging the latest gap-filled MODIS snow cover dataset and multi-source climate variables. The findings provide critical scientific insights into snow cover dynamics over the MP, offering a foundational reference for water resources management, ecosystem conservation, and climate adaptation strategies amid rapid regional climate change.

Utilizing MOD10A1F snow cover products and a decision tree algorithm, this study revealed pronounced spatiotemporal heterogeneity in SCP across the MP during the 2000–2022 hydrological years. D_o, D_e, and D_d exhibited significant regional variations, with 23-year average values of 279.69 ($\pm$81.87) DOY for D_o, 109.13 ($\pm$45.25) DOY for D_e, and 166.29 ($\pm$71.79) days for D_d across the MP in this period. Trend analysis revealed a negligible advance in D_o (-0.03 days yr^{-1}, $p > 0.05$), a significant advancement in D_e (-0.29 days yr^{-1}, $p < 0.01$), and a notable shortening of D_d (-0.26 days yr^{-1}, $p < 0.05$) over the period. Among these, D_e emerged as the primary driver of SCP changes, with its trend magnitude and statistical significance underscoring its dominant role in shaping SCP dynamics and hydrological responses across the MP.

Comprehensive attribution analysis reveals that variations in temperature, precipitation, snow depth, and net shortwave radiation significantly influenced SCP across the MP during the 2000–2022 hydrological years. Specifically, changes in D_o were primarily driven by SW_a (61.07%), P_a (31.27%), and T_a (0.49%), while fluctuations in D_e stemmed predominantly from SW_m (47.72%), T_m (41.22%), and SD_a (22.15%). A cross-comparison of D_o and D_e attribution analyses confirms that shortwave net radiation emerges as the key determinant of SCP anomalies across the MP, underscoring its dominant role in modulating both D_o and D_e dynamics. While precipitation, snow depth, and temperature also exerted significant influences, their effects were secondary to radiation-driven processes. The interplay of these factors introduces complexity and uncertainty into SCP projections, highlighting the need for multi-factor modeling to improve predictive accuracy in this climatically sensitive region.

While previous studies [13,14,18] have investigated the distribution and drivers of SCP at continental scales, this research advances our understanding by resolving recent SCP dynamics across the MP at unprecedented regional and subregional scales (500 m spatial resolution; daily temporal coverage) amid rapid climate change (2000–2022). Moreover, the attribution analysis results of SCP changes on the MP are significantly different from those in the NH. The study identifies that phase transitions of the IPO and AMO trigger mid-latitude atmospheric teleconnection pathways, which favor the development of persistent anticyclonic circulation over the MP. This circulation regime reduces cloud cover by 15–20% and enhances downward shortwave radiation by 0.38 Wm^{-2} yr^{-1} ($p < 0.01$), directly accelerating D_e and suppressing snow depth trends. These mechanisms contrast with NH studies, which often emphasize melt-season temperature as the primary driver [52]. This divergence highlights the unique sensitivity of the MP to radiation–teleconnection feedback, where anticyclonic circulation amplifies solar energy absorption via reduced albedo, creating a self-reinforcing cycle of warming and snow cover decline. The findings not only resolve the fundamental discrepancy in SCP attribution between regional and continental scales but also underscore the necessity of integrating local-scale radiation processes and large-scale climate oscillations in future SCP research. For instance, incor-

porating IPO/AMO indices into regional climate models could improve predictions of snowmelt timing and water resource availability in data-sparse arid regions.

Author Contributions: Conceptualization, X.C.; methodology, X.C.; software, X.C. and S.L.; validation, X.C. and S.L.; formal analysis, X.C.; investigation, X.C.; resources, S.L.; data curation, X.C. and S.L.; writing—original draft preparation, X.C.; writing—review and editing, X.C. and S.L.; visualization, X.C. and S.L.; supervision, X.C.; project administration, X.C.; funding acquisition, X.C. All authors have read and agreed to the published version of the manuscript.

Funding: This research was jointly supported by the Comprehensive Survey of Biodiversity over the Mongolian Plateau (No. 2019FY102001) and the National Key R&D Program of China (2022YFF0711603).

Data Availability Statement: The snow cover data are openly available at https://nsidc.org/data/mod10a1f/versions/61 (accessed on 30 June 2020); the snow depth observations are openly available at https://www.ncei.noaa.gov/access/metadata/landing-page/bin/iso?id=gov.noaa.ncdc:C00516 (accessed on 30 June 2020). Other data will be made available on request.

Acknowledgments: We greatly appreciate the efforts of the National Snow and Ice Data Center and National Centers for Environmental Information in making MOD10A1F and daily snow depth observations publicly accessible.

Conflicts of Interest: The authors declare no conflicts of interest.

Abbreviations

The following abbreviations are used in this manuscript:

MP	Mongolian Plateau
NH	Northern Hemisphere
MODIS	Moderate Resolution Imaging Spectroradiometer
MOD10A1F	MODIS daily cloud-gap-filled snow cover product
NDSI	Normalized Difference Snow Index
CGF	Cloud-gap-filled
CERES	Clouds and the Earth's Radiant Energy System
ERA5-Land	European Center for Medium-Range Weather Forecasts Reanalysis v5-Land
SCP	Snow cover phenology
D_o	Snow onset date
D_e	Snow end date
D_d	Snow duration days
DOY	Day of Year
IPO	Pacific Decadal Oscillation
AMO	Atlantic Multidecadal Oscillation
T_a	Accumulation-season averaged 2 m air temperature
P_a	Accumulation-season averaged total precipitation
SW_a	Accumulation-season averaged net shortwave radiation
SD_a	Accumulation-season averaged snow depth
T_m	Melting-season averaged 2 m air temperature
SW_m	Melting-season averaged net shortwave radiation

References

1. Barnett, T.; Adam, J.; Lettenmaier, D. Potential impacts of a warming climate on water availability in snow-dominated regions. *Nature* **2005**, *438*, 303–309. [CrossRef] [PubMed]
2. Zaremehrjardy, M.; Victor, J.; Park, S.; Smerdon, B.; Alessi, D.S.; Faramarzi, M. Assessment of snowmelt and groundwater-surface water dynamics in mountains, foothills, and plains regions in northern latitudes. *J. Hydrol.* **2022**, *606*, 127449. [CrossRef]
3. Zhang, X.; Sa, C.; Hai, Q.; Meng, F.; Luo, M.; Gao, H.; Zhang, H.; Yin, C.; Zhang, Y.; Sun, H. Quantifying the Effects of Snow on the Beginning of Vegetation Growth in the Mongolian Plateau. *Remote Sens.* **2023**, *15*, 1245. [CrossRef]

4. Chen, X.; Yang, Y. Observed earlier start of the growing season from middle to high latitudes across the Northern Hemisphere snow-covered landmass for the period 2001–2014. *Environ. Res. Lett.* **2020**, *15*, 034042. [CrossRef]
5. Miao, L.; Liu, Q.; Fraser, R.; He, B.; Cui, X. Shifts in vegetation growth in response to multiple factors on the Mongolian Plateau from 1982 to 2011. *Phys. Chem. Earth.* **2015**, *87-88*, 50–59. [CrossRef]
6. Li, C.; Xu, X.; Du, H.; Du, D.; Leal Filho, W.; Wang, J.; Bao, G.; Ji, X.; Yin, S.; Bao, Y.; et al. Potential impacts of climate extremes on snow under global warming conditions in the Mongolian Plateau. *Int. J. Clim. Change Str.* **2022**, *14*, 425–439. [CrossRef]
7. Chen, X.; Yang, Y.; Yin, C. Contribution of Changes in Snow Cover Extent to Shortwave Radiation Perturbations at the Top of the Atmosphere over the Northern Hemisphere during 2000–2019. *Remote Sens.* **2021**, *13*, 4938. [CrossRef]
8. Chen, X.; Liang, S.; Cao, Y. Satellite observed changes in the Northern Hemisphere snow cover phenology and the associated radiative forcing and feedback between 1982 and 2013. *Environ. Res. Lett.* **2016**, *11*, 084002. [CrossRef]
9. Wayand, N.; Lundquist, J.; Clark, M. Modeling the influence of hypsometry, vegetation, and storm energy on snowmelt contributions to basins during rain-on-snow floods. *Water Resour. Res.* **2015**, *51*, 8551–8569. [CrossRef]
10. Di Marco, N.; Avesani, D.; Righetti, M.; Zaramella, M.; Majone, B.; Borga, M. Reducing hydrological modelling uncertainty by using MODIS snow cover data and a topography-based distribution function snowmelt model. *J. Hydrol.* **2021**, *599*, 126020. [CrossRef]
11. Tachiiri, K.; Shinoda, M.; Klinkenberg, B.; Morinaga, Y. Assessing Mongolian snow disaster risk using livestock and satellite data. *J. Arid Environ.* **2008**, *72*, 2251–2263. [CrossRef]
12. Ma, N.; Yu, K.; Zhang, Y.; Zhai, J.; Zhang, Y.; Zhang, H. Ground observed climatology and trend in snow cover phenology across China with consideration of snow-free breaks. *Clim. Dynam.* **2020**, *55*, 2867–2887. [CrossRef]
13. Choi, G.; Robinson, D.A.; Kang, S. Changing Northern Hemisphere Snow Seasons. *J. Clim.* **2010**, *23*, 5305–5310. [CrossRef]
14. Chen, X.; Yang, Y.; Ma, Y.; Li, H. Distribution and Attribution of Terrestrial Snow Cover Phenology Changes over the Northern Hemisphere during 2001–2020. *Remote Sens.* **2021**, *13*, 1843. [CrossRef]
15. Tang, Z.; Deng, G.; Hu, G.; Zhang, H.; Pan, H.; Sang, G. Satellite observed spatiotemporal variability of snow cover and snow phenology over high mountain Asia from 2002 to 2021. *J. Hydrol.* **2022**, *61*, 128438. [CrossRef]
16. Wang, L.; Derksen, C.; Brown, R.; Markus, T. Recent changes in pan-Arctic melt onset from satellite passive microwave measurements. *Geophys. Res. Lett.* **2013**, *40*, 522–528. [CrossRef]
17. Brown, R.; Derksen, C.; Wang, L. A multi-data set analysis of variability and change in Arctic spring snow cover extent, 1967–2008. *J. Geophys. Res.* **2010**, *115*, D16111. [CrossRef]
18. Chen, X.; Liang, S.; Cao, Y.; He, T.; Wang, D. Observed contrast changes in snow cover phenology in northern middle and high latitudes from 2001–2014. *Sci. Rep.* **2015**, *5*, 16820. [CrossRef]
19. Peng, S.; Piao, S.; Ciais, P.; Friedlingstein, P.; Zhou, L.; Wang, T. Change in snow phenology and its potential feedback to temperature in the Northern Hemisphere over the last three decades. *Environ. Res. Lett.* **2013**, *8*, 014008. [CrossRef]
20. Brown, R.D.; Robinson, D.A. Northern Hemisphere spring snow cover variability and change over 1922–2010 including an assessment of uncertainty. *Cryosphere* **2011**, *5*, 219–229. [CrossRef]
21. Song, Y.; Li, Z.; Zhou, Y.; Bi, X.; Sun, B.; Xiao, T.; Suo, L.; Zhang, W.; Xiao, Z.; Wang, C. The Influence of Solar Activity on Snow Cover over the Qinghai–Tibet Plateau and Its Mechanism Analysis. *Atmosphere* **2022**, *13*, 1499. [CrossRef]
22. Xia, Y.-Y.; Chun, X.; Dan, D.; Liu, H.-Y.; Zhou, H.-J.; Wan, Z.-Q. Abrupt change of winter temperature over the Mongolian Plateau during 1961–2017. *J. Mt. Sci.* **2023**, *20*, 996–1009. [CrossRef]
23. Li, Y.; Gong, H.; Chen, W.; Wang, L.; Wu, R.; Dong, Z.; Piao, J.; Ma, K. Summer precipitation variability in the Mongolian Plateau and its possible causes. *Global Planet. Change* **2023**, *228*, 104189. [CrossRef]
24. Xia, Y.; Dan, D.; Liu, H.; Zhou, H.; Wan, Z. Spatiotemporal Distribution of Precipitation over the Mongolian Plateau during 1976–2017. *Atmosphere* **2022**, *13*, 2132. [CrossRef]
25. Frei, A.; Tedesco, M.; Lee, S.; Foster, J.; Hall, D.K.; Kelly, R.; Robinson, D.A. A review of global satellite-derived snow products. *Adv. Space Res.* **2012**, *50*, 1007–1029. [CrossRef]
26. Hall, D.; Riggs, G. MODIS/Terra CGF Snow Cover Daily L3 Global 500m SIN Grid, Version 61. Available online: https://nsidc.org/data/mod10a1/versions/61 (accessed on 15 June 2023).
27. Riggs, G.; Hall, D.; Salomonson, V. MODIS Snow Products User Guide Collection 5. Available online: https://modis-snow-ice.gsfc.nasa.gov/uploads/sug_c5.pdf (accessed on 15 June 2023).
28. Riggs, G.; Hall, D.; Román, M. MODIS Snow Products Collection 6.1 User Guide. Available online: https://nsidc.org/data/documentation/modis-snow-products-collection-61-user-guide (accessed on 10 July 2024).
29. Wang, X.; Wu, C.; Peng, D.; Gonsamo, A.; Liu, Z. Snow cover phenology affects alpine vegetation growth dynamics on the Tibetan Plateau: Satellite observed evidence, impacts of different biomes, and climate drivers. *Agr. Forest Meteorol.* **2018**, *256–257*, 61–74. [CrossRef]
30. Tomaszewska, M.; Nguyen, L.; Henebry, G. Land surface phenology in the highland pastures of montane Central Asia: Interactions with snow cover seasonality and terrain characteristics. *Remote Sens. Environ.* **2020**, *240*, 11167. [CrossRef]

31. Muñoz-Sabater, J.; Dutra, E.; Agustí-Panareda, A.; Albergel, C.; Arduini, G.; Balsamo, G.; Boussetta, S.; Choulga, M.; Harrigan, S.; Hersbach, H.; et al. ERA5-Land: A state-of-the-art global reanalysis dataset for land applications. *Earth Syst. Sci. Data* **2021**, *13*, 4349–4383. [CrossRef]
32. Xin, Y.; Yang, Y.; Chen, X.; Yue, X.; Liu, Y.; Yin, C. One-kilometre monthly air temperature and precipitation product over the Mongolian Plateau for 1950–2020. *Int. J. Climatol.* **2023**, *43*, 3877–3891. [CrossRef]
33. Xin, Y.; Yang, Y.; Chen, X.; Yue, X.; Liu, Y.; Yin, C. Evaluation of IMERG and ERA5 precipitation products over the Mongolian Plateau. *Sci. Rep.* **2022**, *12*, 21776. [CrossRef]
34. Xiao, L.; Che, T.; Dai, L. Evaluation of Remote Sensing and Reanalysis Snow Depth Datasets over the Northern Hemisphere during 1980–2016. *Remote Sens.* **2020**, *12*, 3253. [CrossRef]
35. Fukami, H.; Kojima, K.; Aburakawa, H. The Extinction and Absorption of Solar Radiation Within a Snow Cover. *Ann. Glaciol.* **1985**, *6*, 118–122. [CrossRef]
36. Qu, X.; Hall, A. Assessing Snow Albedo Feedback in Simulated Climate Change. *J. Clim.* **2006**, *19*, 2617–2630. [CrossRef]
37. Loeb, N.; Doelling, D.; Wang, H.; Su, W.; Nguyen, C.; Corbett, J.; Liang, L.; Mitrescu, C.; Rose, F.; Kato, S. Clouds and the Earth's Radiant Energy System (CERES) Energy Balanced and Filled (EBAF) Top-of-Atmosphere (TOA) Edition-4.0 Data Product. *J. Clim.* **2018**, *31*, 895–918. [CrossRef]
38. Ma, Q.; Wang, K.; Wild, M. Impact of geolocations of validation data on the evaluation of surface incident shortwave radiation from Earth System Models. *J. Geophys. Res. Atmos.* **2015**, *120*, 6825–6844. [CrossRef]
39. Zhang, X.; Lu, N.; Jiang, H.; Yao, L. Evaluation of Reanalysis Surface Incident Solar Radiation Data in China. *Sci. Rep.* **2020**, *10*, 3494. [CrossRef] [PubMed]
40. Brutel-Vuilmet, C.; Ménégoz, M.; Krinner, G. An analysis of present and future seasonal Northern Hemisphere land snow cover simulated by CMIP5 coupled climate models. *Cryosphere* **2013**, *7*, 67–80. [CrossRef]
41. Kreyszig, E. *Advanced Engineering Mathematics*; Wiley: Jefferson City, MO, USA, 1979; pp. 1014–1015.
42. He, B.; Tuya, W.; Qinchaoketu, S.; Nanzad, L.; Yong, M.; Kesi, T.; Sun, C. Climate Change Characteristics of Typical Grassland in the Mongolian Plateau from 1978 to 2020. *Sustainability* **2022**, *14*, 16529. [CrossRef]
43. Cai, Q.; Chen, W.; Chen, S.; Xie, S.; Piao, J.; Ma, T.; Lan, X. Recent pronounced warming on the Mongolian Plateau boosted by internal climate variability. *Nat. Geosci.* **2024**, *17*, 181–188. [CrossRef]
44. Na, Y.T.; Qin, F.Y.; Jia, G.S.; Yang, J.; Bao, Y. Change trend and regional differentiation of precipitation over the Mongolian Plateau in recent 54 years. *Arid Land Geogr.* **2019**, *42*, 1253–1261.
45. Brun, E.; Vionnet, V.; Boone, A.; Decharme, B.; Peings, Y.; Valette, R.; Karbou, F.; Morin, S. Simulation of Northern Eurasian Local Snow Depth, Mass, and Density Using a Detailed Snowpack Model and Meteorological Reanalyses. *J. Hydrometeor.* **2013**, *14*, 203–219. [CrossRef]
46. Feld, S.I.; Cristea, N.C.; Lundquist, J.D. Representing atmospheric moisture content along mountain slopes: Examination using distributed sensors in the Sierra Nevada, California. *Water Resour. Res.* **2013**, *49*, 4424–4441. [CrossRef]
47. Zhang, P.; Jeong, J.; Yoon, J.; Kim, H.; Wang, S.; Linderholm, H.; Fang, K.; Wu, X.; Chen, D. Abrupt shift to hotter and drier climate over inner East Asia beyond the tipping point. *Science* **2020**, *370*, 1095–1099. [CrossRef] [PubMed]
48. Wang, T.; Peng, S.; Ottlé, C.; Ciais, P. Spring snow cover deficit controlled by intraseasonal variability of the surface energy fluxes. *Environ. Res. Lett.* **2015**, *10*, 024018. [CrossRef]
49. Batrak, Y.; Muller, M. On the warm bias in atmospheric reanalyses induced by the missing snow over Arctic sea-ice. *Nat. Commun.* **2019**, *10*, 4170. [CrossRef]
50. Peers, M.; Majchrzak, Y.; Menzies, A.; Studd, E.; Bastille-Rousseau, G.; Boonstra, R.; Humphries, M.; Jung, T.; Kenney, A.; Krebs, C.; et al. Climate change increases predation risk for a keystone species of the boreal forest. *Nat. Clim. Change* **2020**, *10*, 1149–1153. [CrossRef]
51. Wang, X.; Wang, T.; Guo, H.; Liu, D.; Zhao, Y.; Zhang, T.; Liu, Q.; Piao, S. Disentangling the mechanisms behind winter snow impact on vegetation activity in northern ecosystems. *Glob. Chang. Biol.* **2018**, *24*, 1651–1662. [CrossRef] [PubMed]
52. Allchin, M.I.; Déry, S.J. Shifting Spatial and Temporal Patterns in the Onset of Seasonally Snow-Dominated Conditions in the Northern Hemisphere, 1972–2017. *J. Clim.* **2019**, *32*, 4981–5001. [CrossRef]
53. Hall, D.K.; Riggs, G.A.; DiGirolamo, N.E.; Román, M.O. Evaluation of MODIS and VIIRS cloud-gap-filled snow-cover products for production of an Earth science data record. *Hydrol. Earth Syst. Sc.* **2019**, *23*, 5227–5241. [CrossRef]
54. Yuan, Y.; Li, B.; Gao, X.; Liu, W.; Li, Y.; Li, R. Validation of Cloud-Gap-Filled Snow Cover of MODIS Daily Cloud-Free Snow Cover Products on the Qinghai–Tibetan Plateau. *Remote Sens.* **2022**, *14*, 5642. [CrossRef]

Disclaimer/Publisher's Note: The statements, opinions and data contained in all publications are solely those of the individual author(s) and contributor(s) and not of MDPI and/or the editor(s). MDPI and/or the editor(s) disclaim responsibility for any injury to people or property resulting from any ideas, methods, instructions or products referred to in the content.